Model Parameter Estimation and Tissue Mixture Segmentation by a MAP-EM Algorithm

Zhengrong Liang*, *Fellow*, *IEEE*, Su Wang, Hongye Lu, and Jing Wang

Abstract*—Quantitative volumetric measurement and feature analysis for various clinical applications require image segmentation. Most important clinical features are derived from the borders of a region of interest, which reflects the shape characteristics and volumetric variation of the target. The partial volume (PV) effect renders a significant error for current hard segmentation which assigns a single tissue label to each image voxel. We have proposed an expectation-maximization (EM) framework for soft image segmentation which aims to quantify the tissue mixture percentages in each voxel. By imposing *a priori* Markov random field (MRF) penalty on the spatial distribution of each tissue mixture, the algorithm searches a maximum *a posteriori* (MAP) solution for the tissue model parameters of the given image and the tissue mixture percentages in each voxel. This work studied the sensitivity of the iterative MAP-EM algorithm to the initial estimate and the properties of its convergence for the estimation of the model parameters and tissue mixtures in the presence of noise. By computer simulations, it was found that the estimation of the model parameters is not sensitive to the parameters' initial estimate (even with greater than 100% error) if the initial estimate of the tissue mixtures is within 10% error from the phantom values. The MRF penalty on the tissue mixture spatial distribution is necessary to ensure the convergence of the iterative tissue mixture estimation in the case of noise level proportional to mean (i.e., similar to Poisson noise). The noise level and initial estimate error are fully within practical conditions, demonstrating that the MAP-EM algorithm is potentially valid in practice. It provides a theoretical or deterministic solution to the PV effect, and its successful implementation could improve quantitative volumetric and feature analyses.

I. Introduction

Image segmentation plays an important role in quantitative analysis of medical images for various clinical applications. Traditional image segmentation algorithms cluster all image voxels into several groups and assign a unique label to each group. Each label indicates a specific tissue type for those voxels inside the corresponding group. Due to limited spatial resolution of the imaging equipment, not all voxels in each labeled group contain the same tissue type, especially for those voxels near tissue borders which are most likely to contain more than one tissue type. This partial volume (PV) effect causes a noticeable error in the traditional hard image segmentation and compromises volumetric analysis in clinical applications, e.g., in evaluation of multiple scloresis with congnitive impairment [1]. Improvement has been observed by soft image segmentation, which models the probability or likelihood of an observed datum belonging to a tissue label [1-4]. These soft segmentation algorithms [1-4] can reduce the PV effect to some degree. However, since they still assign a discrete tissue label to each voxel (where the PV effect is modeled indirectly via the likelihood cost fucntion of the image data), their improvement was shown to be limited [1-4]. This is expected by their indirect modeling of the PV effect. Another class of soft image segmentation utilizes the fuzzy C-mean cost function to indicate the membership of voxels in each group, where the likelihood of a voxel belonging to its group is measured by the Euclidean distance [5, 6]. This class of soft segmentation algorithms faces the same limitation as that class [1-4] due to the same reason of indirect modeling of the PV effect.

Directly modeling different tissue types inside each voxel for PV image segmentation is desired and has been a challenging task due to insufficient measurements to determine the percentages of different tissue types in each voxel [7-10]. Recently, Leemput *et al*. [11] presented a PV image segmentation algorithm that directly determines different tissue components in each voxel by down-sampling that voxel. For example, a voxel may be halved in three dimentions, resulting in eight subvoxels. These eight subvoxels are labeled in a similar manner as in the traditional hard segmentation. If four subvoxels are labeled as tissue type 1, two as tissue type 2, and the remaining two as tissue type 3, then the original voxel contains 50% of tissue type 1, 25% of tissue type 2 and 25% of tissue type 3. Theoretically, this discrete PV image segmentation would approach to an accurate solution when the down-sampling is repeated infinite times, resulting in an infinite number of down-sampled subvoxels to be labeled. In practice, such down sampling is not attainable. In this paper, we present

*This work was supported in part by the NIH National Cancer Institute under Grant # CA082402.

Z. Liang is with the Departments of Radiology and Computer Science, State University of New York, Stony Brook, NY 11794, USA, Tel: 631-444-7837; (jzl@mil.sunysb.edu).

S. Wang is with the Department of Radiology, State University of New York, Stony Brook NY 11794 USA.

H. Lu is with the Department of Radiology, State University of New York, Stony Brook NY 11794 USA.

J. Wang is with the Department of Radiology, State University of New York, Stony Brook NY 11794 USA..

an alternative approach which determines the percentages of different tissue mixtures inside each voxel in a continuous space (without discrete labels) [12] and investigate its performance by numerical simulations.

II. Methods

A. Statistical Model of Image Data

Let the acquired image **Y** be represented by a column vector in the form of $\{ Y_i,\ i = 1, \ldots, I \}$, where I denotes the total number of voxels in the image. Each Y_i is an observation of an individual random variable with mean $\overline{Y}_i$ and variance σ_i^2, i.e.,

$$Y_i = \overline{Y}_i + n_i, \tag{1}$$

where n_i represents the noise associated with observation Y_i. If noise n_i is assumed as statistically mutually independent among the I voxels, then given the mean and variance distributions $\{ \overline{Y}_i \}$ and $\{ \sigma_i^2 \}$ respectively, the conditional probability distribution of the acquired image Y can be described by

$$p(\mathbf{Y} \mid \{\overline{Y}_i\}, \{\sigma_i^2\}) = \prod_{i=1}^{I} p(Y_i \mid \overline{Y}_i, \sigma_i^2). \tag{2}$$

In medical imaging applications, **Y** reflects the spatial distribution of K tissue types inside the body. Near the border of different tissue types, there are more than one and probably K tissue types inside each voxel i. Ignorance of the substructures within each voxel will result in the well-known PV effect. Modeling the PV effect is given below.

B. Statistical Model of Tissue Mixtures

Let the contribution of tissue type k in voxel i to the observation of Y_i be denoted by $\{ X_{ik},\ i=1,\ldots,I;\ k=1,\ldots,K \}$. It is obvious that X_{ik} is also an individual random variable with mean $\overline{X}_{ik}$ and variance σ_{ik}^2, i.e.,

$$X_{ik} = \overline{X}_{ik} + n_{ik}, \tag{3}$$

where n_{ik} represents the noise associated with the generally unobservable variable X_{ik}. If noise n_{ik} is assumed as statistically mutually independent among the I voxels and the K tissue types, then given the distributions $\{ \overline{X}_{ik} \}$ and $\{ \sigma_{ik}^2 \}$ respectively, we have

$$p(\mathbf{X} \mid \{\overline{X}_{ik}\}, \{\sigma_{ik}^2\}) = \prod_{i=1}^{I} \prod_{k=1}^{K} p(X_{ik} \mid \overline{X}_{ik}, \sigma_{ik}^2). \tag{4}$$

As a result from equations (1) to (4), we have the following relationship between the acquired image data $\{ Y_i \}$ and the unobservable tissue variables $\{ X_{ik} \}$,

$$Y_i = \sum_{k=1}^{K} X_{ik}, \tag{5}$$

and their related items,

$$\overline{Y}_i = \sum_{k=1}^{K} \overline{X}_{ik}, \quad n_i = \sum_{k=1}^{K} n_{ik} \quad \text{and} \quad \sigma_i^2 = \sum_{k=1}^{K} \sigma_{ik}^2. \tag{6}$$

More specifically, let Z_{ik} be the contribution fraction from tissue type k in voxel i to observation Y_i with conditions of

$$\sum_{k=1}^{K} Z_{ik} = 1 \quad \text{and} \quad 0 \le Z_{ik} \le 1. \tag{7}$$

Furthermore let μ_k and ν_k be the mean and variance respectively of tissue type k fully filling in voxel i and define [11]

$$\overline{X}_{ik} = Z_{ik}\mu_k \quad \text{and} \quad \sigma_{ik}^2 = Z_{ik}\nu_k, \tag{8}$$

then we have the following relationships

$$\overline{Y}_i = \sum_{k=1}^{K} Z_{ik}\mu_k \quad \text{and} \quad \sigma_i^2 = \sum_{k=1}^{K} Z_{ik}\nu_k. \tag{9}$$

The goal of image segmentation with consideration of the PV effect is to estimate the K tissue mixtures, specifically the percentages of different tissue mixtures $\{ Z_{ik},\ k=1,...,K \}$ in each voxel i, under the condition that each tissue type k can be statistically characterized by the conditional probability distribution $p(.|.)$ of (4) via the tissue model parameters $\{ \mu_k, \nu_k \}$. A specific conditional probability distribution is, as an example, described below.

C. Normal Statistics Model

Without loss of generality, we assume that the unobservable random variable X_{ik} for each tissue type k follows a normal distribution. By the relationship of (5), the acquired datum Y_i also follows a normal distribution. This normal statistics model for Y_i is valid in most applications of computed tomography (CT) and magnetic resonance imaging (MRI) [13-15]. Under this statistics model, equation (2) becomes

$$p(\mathrm{Y} \mid \{\mu_k\}, \{v_k\}, \{Z_{ik}\}) = \prod_{i=1}^{I} \frac{1}{\sqrt{2\pi \sum_{k=1}^{K} Z_{ik} v_k}} \exp\left\{ -\frac{(Y_i - \sum_{k=1}^{K} Z_{ik}\mu_k)^2}{2\sum_{k=1}^{K} Z_{ik} v_k} \right\}, \tag{10}$$

and equation (4) becomes

$$p(X \mid \{\mu_k\}, \{v_k\}, \{Z_{ik}\}) = \prod_{i,k=1}^{I,K} \frac{1}{\sqrt{2\pi Z_{ik} v_k}} \exp\left\{ -\frac{(X_{ik} - Z_{ik}\mu_k)^2}{2\, Z_{ik} v_k} \right\} \tag{11}$$

Estimating the tissue percentage parameters $\{ Z_{ik} \}$ and the tissue model parameters $\{ \mu_k, \nu_k \}$ could be performed by maximizing the conditional probability distribution (10) with respect to each corresponding parameter. This would result in a set of nonlinear equations. Solving these non-linear equations can be very challenging even if it is numerically tractable [16]. Given the many-to-one mapping of (5) and the description of the unobservable variables of (11), the expectation maximization (EM) algorithm [17] would be an alternative and effective solution for this parameter estimation problem.

D. An EM Approach to Parameter Estimation Problem

In the EM framework [17], the observation at each voxel *i* or Y_i is considered as an incomplete random variable, while the underline contributions of each tissue type *k*, $\{X_{ik}, k=1,\ldots,K\}$, are considered as complete random variables which reflect the complete tissue mixture information in each voxel. The probability distribution relationship between the incomplete data $\{Y_i\}$ and the complete data $\{X_{ik}\}$ is depicted by the following integral equation under the condition of (5)

$$P(Y_i \mid \{Z_{ik}\},\{\mu_k\},\{\nu_k\}) = \int_{\{Y_i=\sum_{k=1}^{K} X_{ik}\}} P(X_{ik} \mid \{Z_{ik}\},\{\mu_k\},\{\nu_k\})dX \quad (12)$$

where the integral is understood as the summation over all possible configurations of $\{X_{ik}, k=1,\ldots,K\}$, given Y_i. The EM algorithm [17] then seeks the solution of maximizing the conditional probability distribution (11), given the observations $\{Y_i\}$.

The conditional probability distribution (11) is basically a likelihood function given the tissue parameters. A maximum likelihood (ML) solution is usually not acceptable due to the presence of image noise. To overcome this drawback of ML approach, an *a priori* constraint is routinely imposed to ensure the continuity of the underline tissue distribution within the body for a penalized ML (pML) or maximum *a posteriori* (MAP) solution.

E. Prior Model for Tissue Mixture Regularization

The underline tissue distribution is reflected by the tissue fraction distribution, or distribution of $\{Z_{ik}\}$, across the field-of-view (FOV). The tissue fraction distribution can be modeled as a Markov random field (MRF). By a Gibbs functional in the well-established MRF framework, an *a priori* penalty on the tissue mixture parameter Z_{ik} has the following general form of

$$P\left(Z_{ik} \mid \{Z_{ik\varepsilon_i}\}\right) = C^{-1} \times \exp[-\tfrac{1}{2}\beta\, U(Z_{ik} - Z_{ik\varepsilon_i})], \quad (13)$$

where $\{Z_{ik\varepsilon_i}\}$ indicate the surrounding voxels of Z_{ik} in the neighboring system ε_i, *C* is a normalization constant and β is an adjustable parameter controlling the degree of the penalty. The energy function *U*(.) can be written as a quadratic form of

$$U(Z_{ik}) = \sum_{r\in\varepsilon_i} w_{ir} \cdot (Z_{ik} - Z_{rk})^2, \quad (14)$$

where index *r* indicates the neighbors ε_i and w_{ir} is a weighing factor for different orders of the neighbors.

F. An MAP-EM Algorithm for Tissue Mixture Segmentation

Given equations (11)-(14), an EM approach to MAP solution of estimating the tissue mixture percentages $\{Z_{ik}\}$ and the tissue model parameters $\{\mu_k, \nu_k\}$ is presented below.

(1) ***E-step***: This step computes the conditional expectation of the *posteriori* distribution (11) and (13) of the unobservable variables at the *n*-th iteration, given the acquired data $\{Y_i\}$, by

$$Q(\Theta \mid \Theta^{(n)}) = \mathrm{E}[\ln p(\mathrm{X} \mid \Theta) \cdot p(Z) \mid Y, \Theta^{(n)}]$$
$$= -\frac{1}{2}\sum_{i,k}\{\ln(2\pi) + \ln(Z_{ik}\nu_k) + \frac{1}{Z_{ik}\nu_k}[(X_{ik}^2)^{(n)} - 2X_{ik}^{(n)}Z_{ik}\mu_k + Z_{ik}^2\mu_k^2] + \beta U(Z_{ik})\} \quad (15)$$

where parameter set Θ represents the mixture percentages $\{Z_{ik}\}$ and the model parameters $\{\mu_k, \nu_k\}$, and $X_{ik}^{(n)}$ and $(X_{ik}^2)^{(n)}$ are the conditional expectations of X_{ik} and X_{ik}^2 respectively

$$X_{ik}^{(n)} = \mathrm{E}[X_{ik} \mid Y_i, \Theta^{(n)}] = Z_{ik}^{(n)}\mu_k^{(n)} + \frac{(Z_{ik}^{(n)}\nu_k^{(n)})}{\sum_{j=1}^{K}(Z_{ij}^{(n)}\nu_j^{(n)})} \cdot (Y_i - \sum_{j=1}^{K} Z_{ij}^{(n)}\mu_j^{(n)}) \quad (16)$$

$$(X_{ik}^2)^{(n)} = \mathrm{E}[X_{ik}^2 \mid Y_i, \Theta^{(n)}] = (X_{ik}^{(n)})^2 + (Z_{ik}^{(n)}\nu_k^{(n)}) \cdot \frac{\sum_{j\neq k}^{K}(Z_{ij}^{(n)}\nu_j^{(n)})}{\sum_{j=1}^{K}(Z_{ij}^{(n)}\nu_j^{(n)})} \quad (17)$$

where $(X_{ik}^{(n)})^2$ is the square of the *n*-th iterated estimate of $X_{ik}^{(n)}$.

(2) ***M-step***: This step maximizes the conditional expectation of (15) for the (*n*+1)-th iterated estimate of the tissue model parameters and mixture percentages by simply setting the partial derivatives of $Q(\Theta \mid \Theta^{(n)})$ with respect to μ_k, ν_k and Z_{ik} respectively to zero.

For the mean parameter μ_k, we have

$$\frac{\partial Q}{\partial \mu_k}\Big|_{\mu=\mu^{(n+1)}} = 0 \quad => \quad \mu_k^{(n+1)} = \frac{\sum_i X_{ik}^{(n)}}{\sum_i Z_{ik}^{(n)}}. \quad (18)$$

For the variance parameter ν_k, we have

$$\nu_k^{(n+1)} = \frac{1}{I}\sum_i \frac{(X_{ik}^2)^{(n)} - 2X_{ik}^{(n)}Z_{ik}^{(n)}\mu_k^{(n)} + (Z_{ik}^{(n)}\mu_k^{(n)})^2}{Z_{ik}^{(n)}}. \quad (19)$$

For the mixture percentage Z_{ik}, the conditions of (7) shall be considered when taking the partial derivative of $Q(\Theta \mid \Theta^{(n)})$ with respect to Z_{ik}. There is not a simple formula similar to (18) or (19) for $\{Z_{ik}\}$. Below we only present the equations for solution $\{Z_{ik}^{(n+1)}\}$ in different *K* values.

For *K*=1, we have $Z_{i1}^{(n+1)} = Z_{i1}^{(n)} = 1$ from (7), and $Q(\Theta \mid \Theta^{(n)})$ becomes a constant relative to Z_{i1}.

For *K*=2, let $Z_{i1} = \xi$, we have $Z_{i2} = 1-\xi$ from (7), and $Q(\Theta \mid \Theta^{(n)})$ becomes a function of ξ. By setting the partial derivative of $Q(\Theta \mid \Theta^{(n)})$ with respect to ξ to zero, we have the following fifth-order equation to estimate $\xi = Z_{i1}^{(n+1)}$

$$a\xi^5 + b\xi^4 + c\xi^3 + d\xi^2 + e\xi^1 + f = 0 \quad (20)$$

where *a*, *b*, *c*, *d*, *e* and *f* are constants in the equation and have been determined by the estimated results in the *n*-th iteration [12].

For *K*=3, let $Z_{i1} = \xi_1$ and $Z_{i2} = \xi_2$, we have $Z_{i3} = 1 - \xi_1 - \xi_2$ from (7), and $Q(\Theta|\Theta^{(n)})$ becomes a function of both ξ_1 and ξ_2. By setting the partial derivative of $Q(\Theta|\Theta^{(n)})$ with respect to ξ_1 and ξ_2 respectively to zero, we have two fifth-order equations to estimate $Z_{i1}^{(n+1)}$ and $Z_{i2}^{(n+1)}$. The number of fifth-order equations increases to three for *K*=4, four for *K*=5, and *K*-1 for *K* tissue types. It is clearly seen that the mathematical complexity increases dramatically as *K* goes beyond two.

The numerical complexity can be dramatically reduced if the conditional expectation (15) can be approximated as a quadratic form. This approximation can be achieved by allowing the terms of $\sigma_{ik}^2 = Z_{ik}\nu_k$ in (15) to be estimated from the current-iterated results, i.e., $\sigma_{ik}^2 = Z_{ik}^{(n)}\nu_k^{(n)}$, and by re-normalizing the penalized likelihood function with an adaptive factor $C^{(n)}$ in (13). By this quadratic approximation, the solution for *K*=2 is given by the following close-form formula [18].

$$Z_{i1}^{(n+1)} = \frac{X_{i1}^{(n)}(\sigma_{i2}^2)^{(n)}\mu_1^{(n)} + (\mu_2^{(n)})^2(\sigma_{i1}^2)^{(n)} - X_{i2}^{(n)}(\sigma_{i1}^2)^{(n)}\mu_2^{(n)} + 2\beta(\sigma_{i1}^2)^{(n)}(\sigma_{i2}^2)^{(n)}\sum_r w_{ir}Z_{r1}^{(n)}}{(\mu_1^{(n)})^2(\sigma_{i2}^2)^{(n)} + (\mu_2^{(n)})^2(\sigma_{i1}^2)^{(n)} + 2\beta(\sigma_{i1}^2)^{(n)}(\sigma_{i2}^2)^{(n)}\sum_r w_{ir}} \tag{21}$$

and $Z_{i2}^{(n+1)} = 1 - Z_{i1}^{(n+1)}$, where $X_{ik}^{(n)}$, $(\mu_k)^{(n)}$ and $(\sigma_{ik}^2)^{(n)}$ have been given above. The solution for *K*=3 is determined by two linear equations, instead of two fifth-order equations of (20). The number of linear equations increases to three for *K*=4, four for *K*=5, and *K*-1 for *K* tissue types. Solving the linear equations is much less complex than solving the fifth-order equations.

In the following, we report numerical performance of solving the fifth-order equations, e.g., (20), and the linear equations, e.g., (21), for the tissue mixture percentages $\{Z_{ik}\}$ in terms of accuracy and computing time.

III. Results

A. Data Simulations for K=2

For *K*=2 case in which each voxel contains no more than two tissue types, a two-tissue phantom image of 256×256 array size was generated as follows (the simulation is limited to two dimensions for simplicity). Tissue type 1 had a mean value of $\mu_1 = 100$ units and variance of $\nu_1 = 100$ units. Its percentage distribution $\{Z_{i1}\}$ across the FOV is shown in Figure 1(a). Each pixel in the upper (white) region was fully filled with tissue type 1 (Z_{i1} = 1). The percentage decreased vertically down to zero across the (grey) strip of ten-pixel width in the middle. Each pixel had zero percentage of tissue type 1 (Z_{i1} = 0) below the strip (i.e., the black region). A noise image $\{X_{i1}\}$ of tissue type 1 was simulated with Gaussian noise, where the image density X_{i1} at pixel *i* was given by a Gaussian noise generator [19] with mean of $\overline{X}_{i1} = Z_{i1}\mu_1$ and variance of $\sigma_{i1}^2 = Z_{i1}\nu_1$. Tissue type 2 had a mean value of $\mu_2 = 500$ units and variance of $\nu_2 = 300$ units. Its percentage distribution $\{Z_{i2}\}$ across the FOV is shown in Figure 1(b). A noise image $\{X_{i2}\}$ of tissue type 2 was simulated with Gaussian noise by the same procedure as simulating the noise image of tissue type 1 above. Adding these two noise images together results in the observable noise image $\{Y_i\}$, which is shown in Figure 1(c).

B. Implementation of Equations (20) and (21)

The MAP-EM algorithm of (18)-(19) with quadratic approximation of (21) was implemented by directly programming these three equations using C++ language. When implementing the algorithm with the mathematically exact formula of (20), we employed the *QR* program (C++ code) in [19] to solve the fifth-order equation while equations (18) and (19) were directly programmed using C++ language as described above. These source codes were complied in a Visual C++ environment on a HP XW8000 PC platform (2.4 GHz CPU and 2.0 GB RAM). The complied programs with equation (20) (or theoretically exact implementation) and equation (21) (or quadratic approximated implementation) each ran up to 60 iterations to ensure that a stable solution is achieved. In our experiments below, a stable solution was observed after ten iterations.

C. Estimation of Tissue Model Parameters $\{\mu_k, \nu_k\}$

We first studied the accuracy of estimators (18) and (19) with known $\{Z_{ik}\}$. By setting the initial model parameters $\{\mu_k^{(0)}, \nu_k^{(0)}\}$ with 99.9% error from the ground truth of $\{\mu_1 = 100, \nu_1 = 100, \mu_2 = 500, \nu_2 = 300\}$ and fixing the mixture percentages $\{Z_{ik}^{(n)}\}$ as the ground truth of Figure 1(a) and Figure 1(b) at all iterations, we obtained the iterated results after thirty iterations $\{\mu_k^{(30)}, \nu_k^{(30)}\}$ as shown in Table 1, where the model parameters of the phantom image were computed over those pixels inside the white and black regions in Figure 1(c) excluding the PV effect (i.e., ignoring the grey strip in the middle). These results indicate that the phantom image with Gaussian noise is accurately simulated, and the estimation of the model parameters is robust regardless of 99.9% initial error.

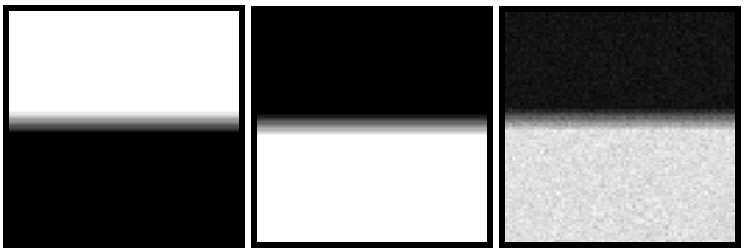

(a) (b) (c)

Figure 1: Simulation of a phantom image of two density levels with PV effect. Picture (a) represents the distribution of $\{Z_{i1}\}$ for tissue type 1. Pixels in the upper (white) region are fully filled with tissue type 1, while pixels in the lower (black) region have zero percentage of tissue type 1. Picture (b) reflects the distribution of $\{Z_{i2}\}$ for tissue type 2. Pixels in the upper (black) region have zero percentage of tissue type 2, while pixels in the lower (white) region are fully filled by tissue type 2. The PV effect occurs between the white and black regions of ten-pixel width in the middle. Picture (c) shows the two-tissue phantom image with Gaussian noise.

We then repeated the above experiment by updating the mixture percentages $\{Z_{ik}^{(n+1)}\}$ with equation (20) and (21) respectively from the initial of $\{Z_{ik}^{(0)}\}$ being the ground truth. The iterated results after thirty iterations are shown in Table 2. The % error reflects the difference of the iterated result from the corresponding ground truth. The updates by equations (20) and (21) generated similar results. There is some difference in the estimate of ν_1 due to a smaller mean and larger variance for tissue type 1 in the phantom image, as compared to that of tissue type 2. This difference was observed in all the experiments performed in this study

	μ_1	μ_2	ν_1	ν_2
Result from the phantom image	100.08	500.04	99.60	296.62
Iterated result with fixed Z_{ik}	100.07	500.02	99.47	297.35

Table 1: Iterated tissue model parameters by the MAP-EM algorithm with comparison to that of the phantom image. β was set to zero to ignore the effect of the penalty.

	err(μ_1)	err(μ_2)	err(ν_1)	err(ν_2)
Theoretical update (20)	0.05%	0.00%	1.41%	2.18%
Approximated update (21)	0.05%	0.00%	0.89%	2.24%

Table 2: Comparison of iterated tissue model parameters using the theoretical solution (20) and the approximated solution (21). β was set to zero to ignore the effect of the penalty.

D. Performance Comparison between Equations (20) and (21)

To show the robustness of the MAP-EM segmentation algorithm for different initial estimates on the mixture percentages, we repeated the above experiment by allowing the initial $\{Z_{ik}^{(0)}\}$ with various % deviations from 10% up to 99.9%. The % deviations were generated by sampling each $Z_{ik}^{(0)}$ using the Gaussian noise generator [19] with a given % standard deviation from its ground truth Z_{ik} in Figure 1. The iterated results after thirty iterations are shown in Table 3. The percentage error of estimating the tissue mixture percentages $\{Z_{ik}\}$ in the table was computed from those pixels in the PV horizontal strip in Figure 1. Because of the penalty, the percentages $\{Z_{ik}\}$ in the single tissue type (white and black) regions of Figure 1 were accurately estimated. Both implementations with exact solution (20) and approximated solution (21) generated similar results.

	err$\{Z_{ik}\}$	err$\{Z_{ik}\}$	err$\{Z_{ik}\}$
Theoretical update (20)	2.23%	2.65%	2.73%
Approximated update (21)	2.39%	2.75%	2.75%

Table 3: Comparison of iterated tissue mixture percentages using the theoretical solution (20) and the approximated solution (21). The results are (from left to right): (a) $\{Z_{ik}^{(0)}\}$ were given while $\{\mu_k^{(0)}, \nu_k^{(0)}\}$ were randomized. (b) $\{Z_{ik}^{(0)}\}$ were randomized while $\{\mu_k^{(0)}, \nu_k^{(0)}\}$ were given. (c) both $\{Z_{ik}^{(0)}\}$ and $\{\mu_k^{(0)}, \nu_k^{(0)}\}$ were randomized. β =0.5.

E. Convergence Comparison between Equations (20) and (21)

The convergence performance of the MAP-EM algorithm using equations (20) and (21) respectively was also studied in the experiments as described in Section III.D above. The convergence is measured by the relative error of

$$\varepsilon(Z_{ik}) = \sum_{i=1}^{I_R} \left| Z_{ik}^{(n)} - Z_{ik}^{(truth)} \right| / I_R \qquad (22)$$

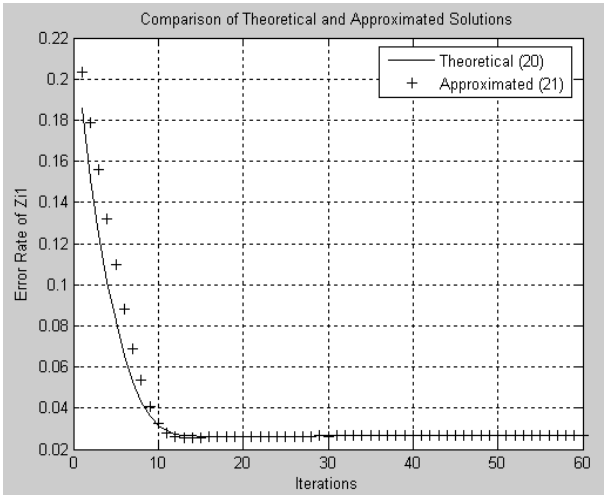

Figure 2: Comparison of iterated tissue mixture percentages against iteration number using the theoretical solution (20) (solid line) and the approximated solution (21) (crosses), where β=0.5 was used. A similar convergence rate was observed for both Z_{i1} and Z_{i2} because of the relationship (7), i.e., $Z_{i2} = 1 - Z_{i1}$.

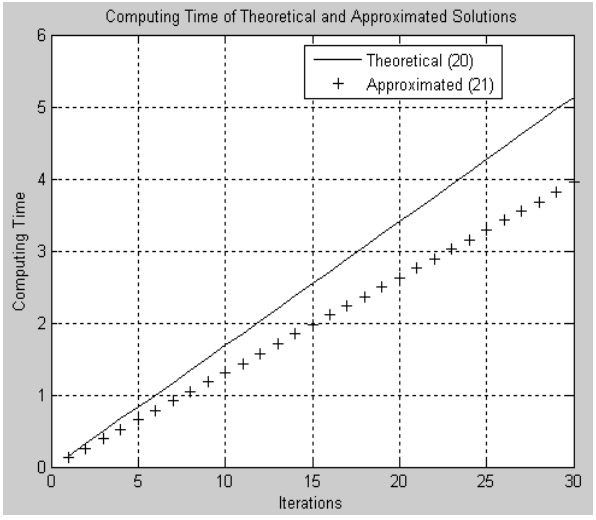

Figure 3: Comparison of computing time (seconds) against iteration number between the theoretical solution (20) (solid line) and the approximated solution (21) (crosses), where β=0.5 was used.

where I_R indicates the number of those pixels inside the PV horizontal strip in Figure 1. Figure 2 shows, as an example, the result when the initial $\{Z_{ik}^{(0)}\}$ had 50% deviation from the ground truth. Similar results were observed for other initial errors on $\{Z_{ik}^{(0)}\}$. A stable solution after ten iterations was observed. The computing time for the iterative process was documented and plotted in Figure 3. The *QR* program for the solution of (20) costs approximately 25% more computing time than the computation of (21) after 30 iterations.

IV. Discussion and Conclusion

In the mathematical derivation of the MAP-EM algorithm, we assumed *K* to be the total number of different tissue types inside the body. The tissue model parameters $\{\mu_k, \nu_k\}$ of these *K* tissue types were estimated using all the image data $\{Y_i\}$ by (18) and (19). In the implementation of (20) and (21) for estimation of the tissue mixture percentages $\{Z_{ik}\}$, only datum Y_i and its neighbors were used. Then the number of tissue types in each voxel varied across the FOV. In other words, the total number of tissue types *K* inside the body can be much greater than two, while the estimators (20) and (21) remain valid if a voxel contains no more than two tissue types. Similarly, a similar estimator will remain valid if a voxel contains no more than three, or four tissue types, despite the total number *K* of tissue types in the body is far beyond three or four.

Estimator (20) is mathematically exact. It is a fifth-order equation and would generate five possible values for each Z_{i1} when the *QR* program in [19] is used. In most cases, the constraint of $0 \le Z_{i1} \le 1$ eliminated the other four possible values. Sometimes we encountered a choice of one from two possible values for Z_{i1} in the range of [0, 1]. In these cases, we chose the one which was closer to the previously iterated value. In contrast, equation (21) determines a value for each Z_{i1} in the range of [0, 1]. However, because the quadratic approximation is made at the *n*-th iteration, then the estimator (21) for $\{Z_{i1}\}$ at the (*n*+1)th iteration is somehow bounded to the result at the *n*-th iteration, causing a slower initial convergence compared to the theoretical solution (20) (see Figure 2). For K>2, the *QR* program is no longer applicable. When the Newton gradient program in [19] was used, a same convergence speed was obtained as that of the quadratic approximation. This is because of the Newton gradient program searches the solution from the *n*-th iterated result, a similar bound to the *n*-th iteration as that in the quadratic approximation. Other numerical methods similar to the *QR* for K>2 would avoid the slower initial convergence and are under investigation. For digital implementation of both the theoretical solution and the quadratic approximation, we modified the condition $0 \le Z_{i1} \le 1$ to be $0.01 \le Z_{i1} \le 0.99$ to avoid Z_{ik} being zero (or avoid numerical instability when Z_{ik} is in the denominator).

Both estimators of the theoretical solution and the quadratic approximation generated similar results for the tissue mixture percentages $\{Z_{ik}\}$, leading to a similar estimate of the tissue model parameters $\{\mu_k, \nu_k\}$ by equations (18) and (19). The computational efficiency was also similar for both estimators when the Newton's gradient program was used to solve the set of fifth-order equations for the theoretical solution. There is no

noticeable benefit to solve a set of fifth-order equations for the tissue mixture percentages, as compared to solving a set of linear equations by the quadratic approximation, unless a more accurate program, similar to or better than the *QR* program, is available to solve the fifth-order equations. Therefore, the quadratic approximation may be a choice for practical applications at present time.

The presented MAP-EM framework is based on the relationship (5) between the observed datum Y_i and the unobservable tissue contributions $\{X_{ik}\}$ inside each voxel *i*. This relationship is different from that of $Y_i = \sum_{k=1}^{K} Z_{ik} X_{ik}$ used in [7-10] for modeling of the PV effect. Because of this difference, the expressions for the data mean and variance of (9) are different from those in [7-10]. Without relationship (5), relation (12) would not hold and, therefore, the EM algorithm [17] could no be applicable. The derived MAP-EM algorithm (18)-(21) computes the tissue mixture percentages and the tissue model parameters in a continuous space and does not assume any voxel size. Therefore it is a mathematical or theoretical solution to the PV effect in image segmentation. Further validation of the algorithm by clinical studies is needed and is in progress.

V. REFERENCES

[1] L. Li, H. Lu, X. Li, W. Huang, A. Tudorica, C. Christodoulou, L. Krupp, and Z. Liang, "MRI volumetric analysis of multiple sclerosis: Methodology and validation", *IEEE Transactions on Nuclear Science*, vol. 50, no. 5, pp. 1686-1692, 2003.

[2] Z. Liang, R. Jaszczak, and E. Coleman, "Parameter estimation of finite mixtures using the EM algorithm and information criteria with application to medical image processing", *IEEE Transactions on Nuclear Science*, vol. 39, no. 4, pp. 1126-1133, 1992.

[3] S. Sanjay-Gopal and T. Hebert, "Bayesian pixel classification using spatially variant finite mixtures and the generalized EM algorithm", *IEEE Transactions on Image Processing*, vol. 7, no. 7, pp. 1014-1028, 1998.

[4] Y. Zhang, M. Brady, and S. Smith, "Segmentation of brain MR images through a hidden Markov random field model and the expectation-maximization algorithm", *IEEE Transactions on Medical Imaging*, vol. 20, no. 1, pp. 45-57, 2001.

[5] D. Pham and J. Prince, "Adaptive fuzzy segmentation of magnetic resonance images", *IEEE Transactions on Medical Imaging*, vol. 18, no. 9, pp. 737-752, 1999.

[6] X. Li, L. Li, H. Lu, and Z. Liang, "A partial volume segmentation of brain magnetic resonance images based on maximum *a posteriori* probability", *Medical Physics*, vol. 32, no. 7, pp. 2337-2345, 2005.

[7] H. Choi, D. Haynor, and Y. Kim, "Partial volume tissue classification of multi-channel magnetic resonance images – A mixel model", *IEEE Transactions on Medical Imaging*, vol. 10, no. 3, pp. 395-407, 1991.

[8] P. Santago and H. Gage, "Quantification of MR brain images by mixture density and partial volume modeling", *IEEE Transactions on Medical Imaging*, vol. 12, no. 3, pp. 566-574, 1993.

[9] P. Santago and H. Gage, "Statistical models of partial volume effect", *IEEE Transactions on Image Processing*, vol. 4, no. 11, pp. 1531-1539, 1995.

[10] K. Blekas, A. Likas, N. Galatsanos, and I. Lagaris, "A spatially constrained mixture model for image segmentation", *IEEE Transactions on Neural Networks*, vol. 16, no. 4, pp. 494-498, 2005.

[11] K. Leemput, F. Maes, D. Vandermeulen, and P. Suetens, "A unifying framework for partial volume segmentation of brain MR images", *IEEE Transactions on Medical Imaging*, vol. 22, no. 1, pp. 105-119, 2000.

[12] Z. Liang, X. Li, D. Eremina, and L. Li, "An EM framework for segmentation of tissue mixtures from medical images", *International Conference of IEEE Engineering in Medicine and Biology*, Cancun, Mexico, pp. 682-685, 2003.

[13] T. Lei and W. Sewchand, "Statistical approach to X-ray CT imaging and its applications in image analysis - Part I and II", *IEEE Transactions on Medical Imaging*, vol. 11, no. 1, pp. 53-69, 1992.

[14] M. Fuderer, "The information content of MR images", *IEEE Transactions on Medical Imaging*, vol. 7, no. 4, pp. 368-380, 1988.

[15] A. Macovski, "Noise in MRI", *Magnetic Resonance in Medicine*, vol. 36, no. 4, pp. 494-497, 1996.

[16] X. Li, D. Eremina, L. Li, and Z. Liang, "Partial volume segmentation of medical images", *Conference Record of IEEE Nuclear Science Society-Medical Imaging Conference*, in CD-ROM, 2003.

[17] A. Dempster, N. Laird, and D. Rubin, "Maximum likelihood from incomplete data via the EM algorithm", *Journal of the Royal Statistics Society*, vol. 39(B), pp. 1-38, 1977.

[18] D. Eremina, X. Li, W. Zhu, J. Wang, and Z. Liang, "Investigation on an EM framework for partial volume image segmentation", *Proceedings of SPIE Medical Imaging*, vol. 6144, pp. D1-D9, 2006.

[19] W. Press, S. Teukolsky, W. Vetterling, and B. Flannnery, "*Numerical Recipes in C: The art of scientific computing*", The Second Edition, Cambridge University Press, pp. 50-51, 1992.